Additive Manufacturing Letters 5 (2023) 100127

Contents lists available at ScienceDirect

Additive Manufacturing Letters

journal homepage: www.elsevier.com/locate/addlet

Blue laser directed energy deposition of aluminum with synchronously enhanced efficiency and quality

An Wang[a,b], Qianglong Wei[a,b], Sheng Luo[a,b], Zijue Tang[a,b], Huihui Yang[a,b], Yi Wu[a,b,c], Chu Lun Alex Leung[d,e], Peter D. Lee[d,e], Haowei Wang[a,b,c], Hongze Wang[a,b,c,*]

[a] State Key Laboratory of Metal Matrix Composites, Shanghai 200240, China
[b] School of Materials Science & Engineering, Shanghai Jiao Tong University, Shanghai 200240, China
[c] Institute of Alumics Materials, Shanghai Jiao Tong University (Anhui), Huaibei 235000, China
[d] Department of Mechanical Engineering, University College London, London WC1E 7JE, United Kingdom
[e] Research Complex at Harwell, Harwell Campus, Oxfordshire OX11 0FA, United Kingdom

ARTICLE INFO

Keywords:
Blue laser directed energy deposition (BL-DED)
Laser absorption rate
Single track
AlSi10Mg/TiB2

ABSTRACT

Directed energy deposition (DED) of aluminum with infrared lasers faces many processing issues, *e.g.,* poor formability, pore formation, high reflectivity, all lowering the productivity. In this paper, we developed and applied a 2 kW high-power (450 nm) blue laser directed energy deposition (BL-DED) of a nano-TiB2 decorated AlSi10Mg composite. The single-track experiment reveals that the required power density of blue laser to form fully melted track is lower than that of an infrared laser (1060 nm). Under the laser power of 900 W with a scanning speed of 4 mm/s, the width and depth of molten pool is approximately 2500 μm and 350 μm respectively with blue laser, while the powders are not fully melted with infrared laser, owing to aluminum's higher absorption at blue laser wavelengths. The area fraction of equiaxed grains accounts for as high as 63% at 4 mm/s. To the best of our knowledge, this result is the highest area fraction of equiaxed grains in a single-track molten pool of DED process. Such a high fraction is mainly due to the low thermal gradient (8×10^5 K/m) of the flat-top blue laser and the refining effect of nano TiB2 particles. Our work demonstrates that high-power blue laser has enhanced both efficiency and build quality compared to DED of aluminum alloys and composites using an infrared laser, which also promises to help process other high-reflectivity materials like copper alloys.

1. Introduction

Additive manufacturing (AM) has become more and more popular in recent years because it can manufacture parts with complex shapes [1], customizing the microstructure and properties for various specific applications [2]. Directed energy deposition (DED), as a generally accepted AM method for metals, is a technique in which a focused energy source is used to fuse materials by melting as they are being deposited [3]. In addition, DED technology has advantages for component repair and surface improvement. [4]. However, challenges such as poor formability and low strength [5,6], exist in DED when processing alloys such as aluminum (Al) [7], copper (Cu) [8,9] etc. Infrared lasers with a wavelength of >1 μm are commonly employed in current DED processing. However, Al alloy has a relatively high reflectivity in the infrared region [10] and often requires a high laser power to process such materials. According to Dausinger and Shen et al. [11], the absorption rate of Al alloys under the infrared laser is merely 5% calculated by the Fresnel absorption equation. In addition, the characteristics of grains in the molten pool are affected by the temperature gradient (G) and solidification growth rate (R). A high temperature gradient under an infrared laser with gaussian distribution can lead to columnar grain growth, which is detrimental to the properties of components [12]. Furthermore, a low energy conversion efficiency can lead to the formation of pores [13] due to limited fusion at low laser power and a violent fluctuation of the molten pool at high laser power, lowering the productivity of DED Al alloys.

One solution is to improve the powder absorbance by adding photothermal additives, *e.g.* reduced graphene oxide [14]. Another effective solution is to find a more suitable laser source. Tumkur et al. [15] found that the Bessel beam stabilizes the internal turbulence and accelerates the solidification speed of the molten pool by reducing the temperature gradient. Meanwhile, Roehling et al. [16] suggested that an elliptical beam can improve the microstructure of materials and reduce the ratio of columnar grains, compared with a gaussian beam. Unfortunately, these methods are all based on infrared lasers and don't address the difficulty that low absorption alloys pose. Alternatively, a laser source with a much shorter wavelength, specifically blue lasers (wavelength

* Corresponding author.
E-mail address: hz.wang@sjtu.edu.cn (H. Wang).

https://doi.org/10.1016/j.addlet.2023.100127
Received 16 August 2022; Received in revised form 5 January 2023; Accepted 4 February 2023

Table 1
Chemical compositions of AlSi10Mg/TiB2.

Element	Si	Mg	Fe	Ti+*B*	Al
Wt. (%)	9.61	0.41	0.13	6	Bal.

of 450 nm), have a much greater absorptivity by Al alloys [17–19]. As a new laser source [20], the advantages of blue laser include a compact structure and a long service life. For some metals, especially the traditional high reflectivity ones (such as Al, Cu), there is a higher absorption rate in blue laser than that in the infrared region. Meanwhile, Wang et al. [10] developed a 250 W high-power blue laser (445 nm) and significantly increased the absorption rate of laser in welding of steel. In addition, Abhishek et al. [21] used a 500 W diode blue laser produced by NUBURU for welding of AISI 316 L stainless steel, finding that the blue laser welding can reduce the discontinuity of the welding area and has excellent mechanical properties. Subsequently, a 1000–1500 W high-power blue laser generator has been developed by Laserline GmbH [22] to carry out the research for copper welding. However, the formability of aluminum matrix composites under blue laser directed energy deposition (BL-DED) is not yet known and the advantage of the blue laser in processing of aluminum has not been proven.

Aluminum alloys and composites have been widely used in industry and high-quality parts fabricated by the DED process is urgently required [23,24]. Here, we first applied a 2 kW high-power BL-DED of nano-TiB2 decorated AlSi10Mg composite. The formability of AlSi10Mg/TiB2 composite under both infrared and blue laser were quantitatively analyzed by both experiment and simulation.

2. Materials and methods

In this experiment, the spherical AlSi10Mg/TiB2 powders prepared by gas atomization were used. The average particle size was 60 μm and the chemical composition is shown in Table 1, expressed by weight score *(wt.%)*. The substrate was cold rolled AlSi10Mg substrate. All experiments were carried out on a machine (*LDM 4030, China*), which can be equipped with different laser devices, such as blue and IR lasers. The beam radius of the laser is the distance between the beam center and the beam edge where the intensity drops to $1/e^2$ (13.5%) of the maximum value. Both laser beams were focused to a beam diameter of 2.5 mm and their intensity profiles were measured by the Charged Coupled Device using the method depicted by [25]. The blue laser has

Table 2
Processing parameters of the single track under blue and infrared lasers.

	Blue laser	Infrared laser
Wavelength (nm)	450	1060
Laser power (W)	900	900
Scanning speed (mm/s)	4, 6, 8, 10	4, 6, 8, 10
Powder feeding rate (g/min)	1.5	1.5
Laser beam diameter (mm)	2.5	2.5
Average power density (W/mm^2)	183.3	183.3

a flat-top distribution whereas the infrared laser has a gaussian distribution. The processing parameters of single-track samples are shown in Table 2. Fig. 1(a) and (e) show the energy distribution of the infrared and blue laser sources respectively, both calculated and plotted in MATLAB. Eq. (1) and (2) are the energy distribution functions of the gaussian laser and flat-top laser, respectively [26,27]:

$$q_{Gaussian}(x,y) = \frac{3Pe_1}{\pi r_1^2} e^{\left(\frac{-3\left(x^2+y^2\right)}{r_1^2}\right)} \tag{1}$$

$$q_{Flat}(x,y) = \frac{Pe_2}{\pi r_1^2} e^{\left(\frac{-\sqrt{x^2+y^2}}{r_1}\right)^n} \tag{2}$$

where $q_{Gaussian}$ and q_{Flat} are the laser energy density of gaussian and flat-top distributions respectively, e_1 is the absorption rate of infrared laser, e_2 is the absorption rate of the blue laser, r_1 represents the beam radius of lasers, P is the laser power, and n is the polynomial order of the flat-topped beam. We adopted the trial-and-error method, validating the equation parameters with the temperature distribution of molten pool detected by paraxial infrared camera. The measured temperature distributions are in good agreement with the calculated ones when $n = 30$.

The microstructures of the single tracks with different scanning speeds v are characterized using an optical microscope (OM) and an electron backscattered diffraction (EBSD) detector under a scanning electron microscope. A Computational Fluid Dynamics (CFD) model is developed to reveal the physical mechanisms using commercial software Flow3D (*Flow Science, USA*) [28]. The simulation domain consists of one layer of powder particles and a substrate, where the dynamic powders are blown to the surface of the substrate, filling the powder domain. The detailed modeling process is in the supplementary document.

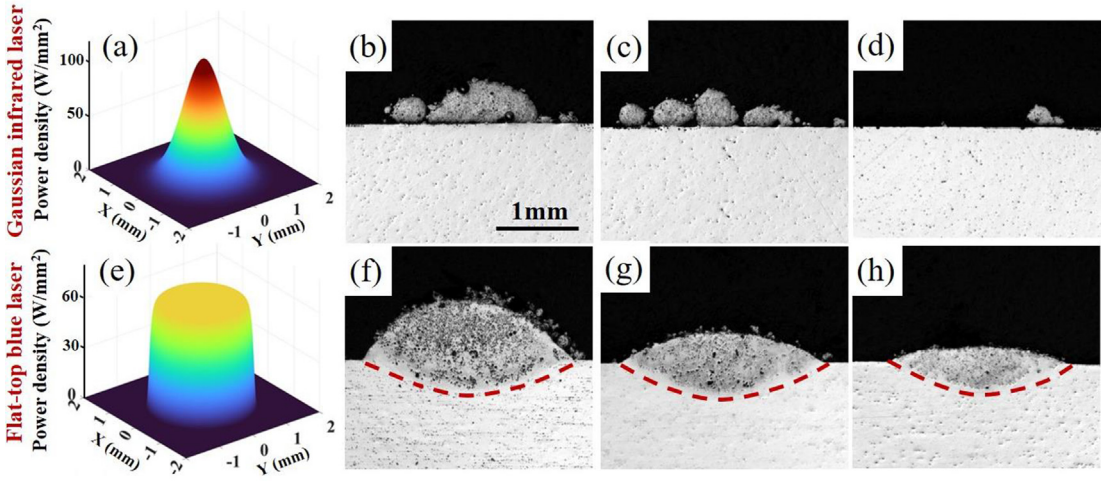

Fig. 1. Numerical visualization of the laser source model and experimental transverse cross-sections of the molten pool at different laser melting parameters: (a) the energy density of a gaussian infrared laser beam, and the molten pool produced by the infrared laser with P = 900 W and v = (b) 4 mm/s, (c) 6 mm/s, and (d) 10 mm/s; (e) the energy density of a flat-top blue laser beam, and the molten pool produced by blue laser at P = 900 W and v = (f) 4 mm/s, (g) 6 mm/s, and (h) 10 mm/s.

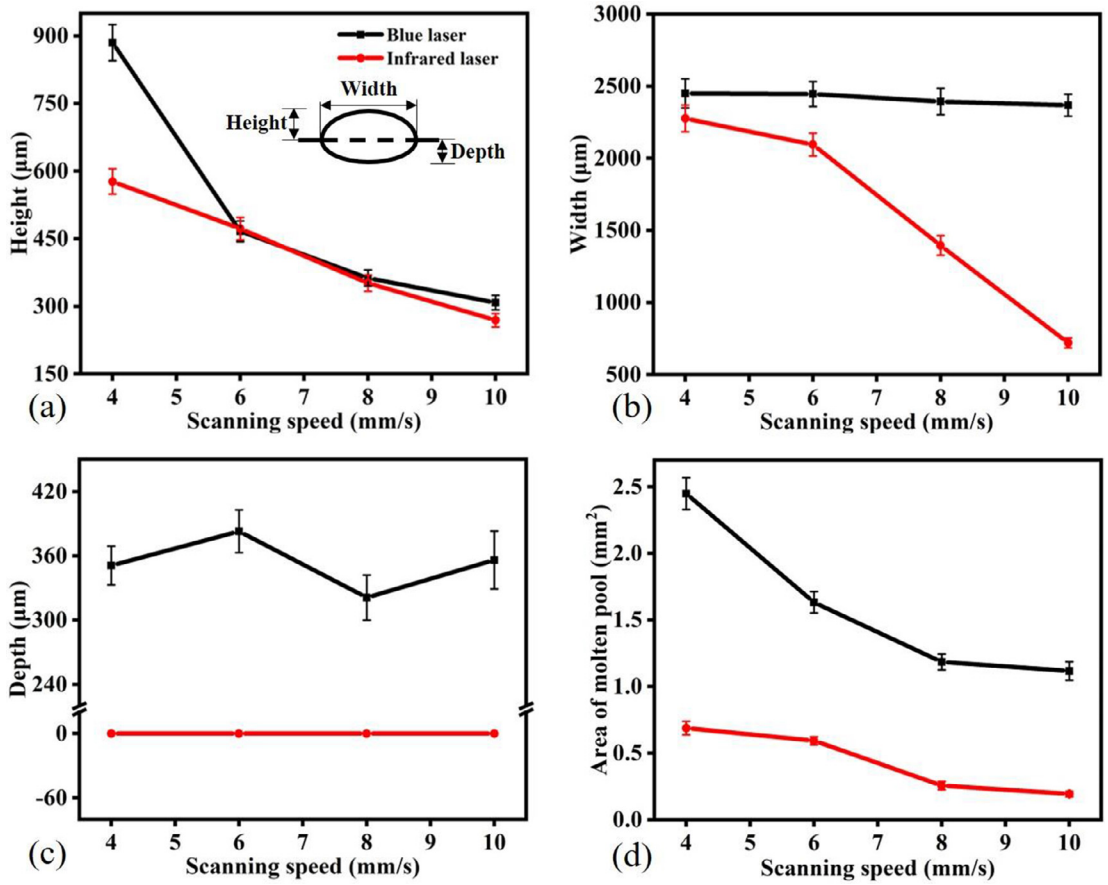

Fig. 2. Effects of laser scanning speed on: (a) height of the molten pool; (b) width; (c) depth and (d) area of molten pool.

3. Results and discussion

3.1. Characteristics of the cross-section of the molten pool

Fig. 1 shows transverse cross-sections of the molten pool using an infrared and a blue laser at different laser melting parameters. Using an infrared laser beam, the powder particles are partially melted at v = 4 and 6 mm/s (Fig. 1b-c). As v increased to 10 mm/s, no distinct molten pool is evident (Fig. 1d). Some of the powder particles do not bind to the substrate, indicating that the substrate did not melt. In contrast, the AlSi10Mg/TiB2 powders are fully melted by the blue laser. Fig. 1 (f-h) shows that all the molten pool geometries exhibit a hemi-spherical shape, indicating the melting process was in a heat conduction mode. These results show that the printability of AlSi10Mg/TiB2 composite using the blue laser is better than that of the infrared laser by DED process. Moreover, there are some black spots of the molten pool under the optical microscope, as shown in Fig. 1 (f-h). These black spots may contain defects, segregation of TiB2 particles, and Si phases that are corroded during etching.

Fig. 2 shows the measurements of molten pool geometries of AlSi10Mg/TiB2 composite using both laser sources. Fig. 2(a)-(d) show the measured height, width, depth and area of molten pool respectively. With increasing v, the height and area of the molten pool decrease under 900 W blue or infrared laser. In general, the molten pool area under the blue laser is much larger than that under the infrared laser. However, the width and depth of the molten pool remain unchanged with increasing v by the blue laser, in which the average width is *ca.* 2500 μm and average depth is *ca.* 350 μm. The width of the molten pool is roughly the same as the blue laser diameter.

3.2. The distribution of grains and single-track simulation

Fig. 3(a), (c), (e) and (g) show EBSD maps of cross-section images of a single-track AlSi10Mg/TiB2 composite under a 900 W blue laser at 4, 6, 8 and 10 mm/s respectively. A distinct transition from columnar to equiaxed grains can be seen from the bottom to the top of the molten pool. From the histogram of equiaxed and columnar grains, the size of the equiaxed grains is mainly below 50 μm, meanwhile there are also larger grains because of continuous heat input. Furthermore, the major size distribution of the large columnar grains is between 20 and 60 μm.

Fig. 4(a), (b), (c) and (d) show the measured area fraction of columnar grains, equiaxed grains and a mixture of both at different scanning speeds. Especially, grains with length to width aspect ratio less than 2 are regarded as equiaxed grains [29,30]. Evidently, the ratios of equiaxed grains are 63%, 60%, 57%, and 55% at scanning speeds of 4, 6, 8, and 10 mm/s, respectively. Fig. 4(e) shows that the area fraction of equiaxed grains reported in the study is the highest among the *ref.* studies [16,30-34]. The high proportion of equiaxed grains will in part be due to the presence of TiB2, as it is a potent grain refiner [35].

The simulation results in Fig. 5(a) and (b) clearly illustrate the molten pool morphology, consistent with the experimental results. Fig. 5(c) and (d) show the temporal evolution of temperature gradient (G) and velocity at the solid-liquid (S/L) interface (R) for BL-DED. Local G and R in the molten pool at a given time are calculated using the specific formula [36] outlined in the supplementary document. The G and R values obtained by simulation are displayed on a solidification map showing the boundaries of the fully columnar, equiaxed, and mixed regions, and the predicted grain structure.

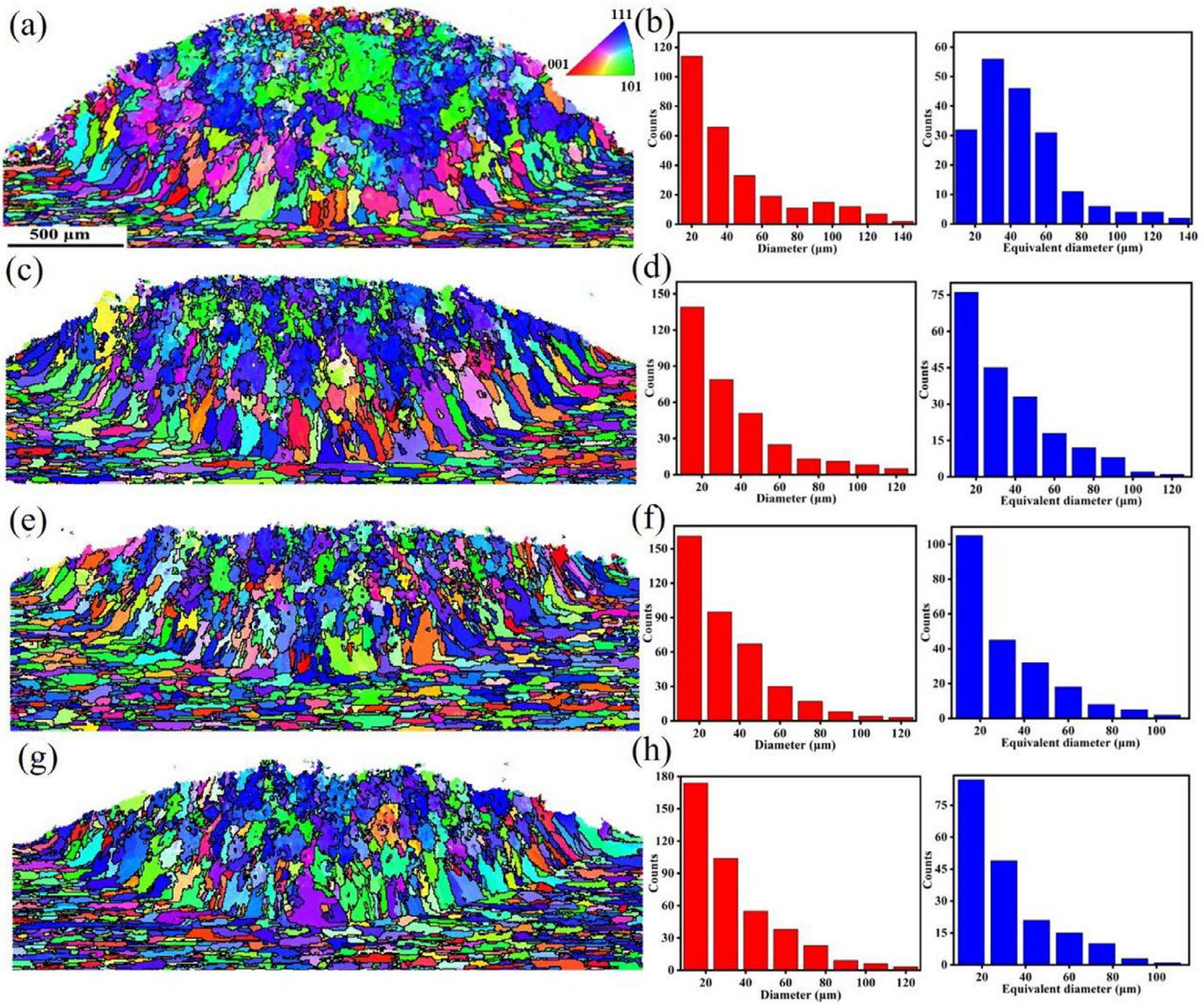

Fig. 3. EBSD maps of AlSi10Mg/TiB2 composite fabricated by the BL-DED: (a), (c), (e), (g) under 900 W blue laser with 4, 6, 8, 10 mm/s (cross section view); (b), (d), (f) and (h) corresponding histogram of equiaxed (red) and columnar grains (blue).

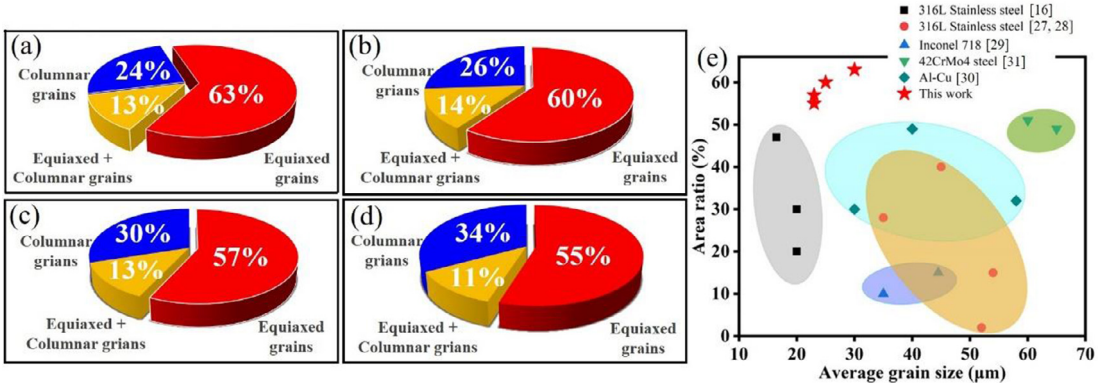

Fig. 4. (a), (b), (c), (d) the area percentage of equiaxed and columnar grains with 4, 6, 8, 10 mm/s respectively, and (e) comparison of area fraction of equiaxed grains of our work and other ref. studies.

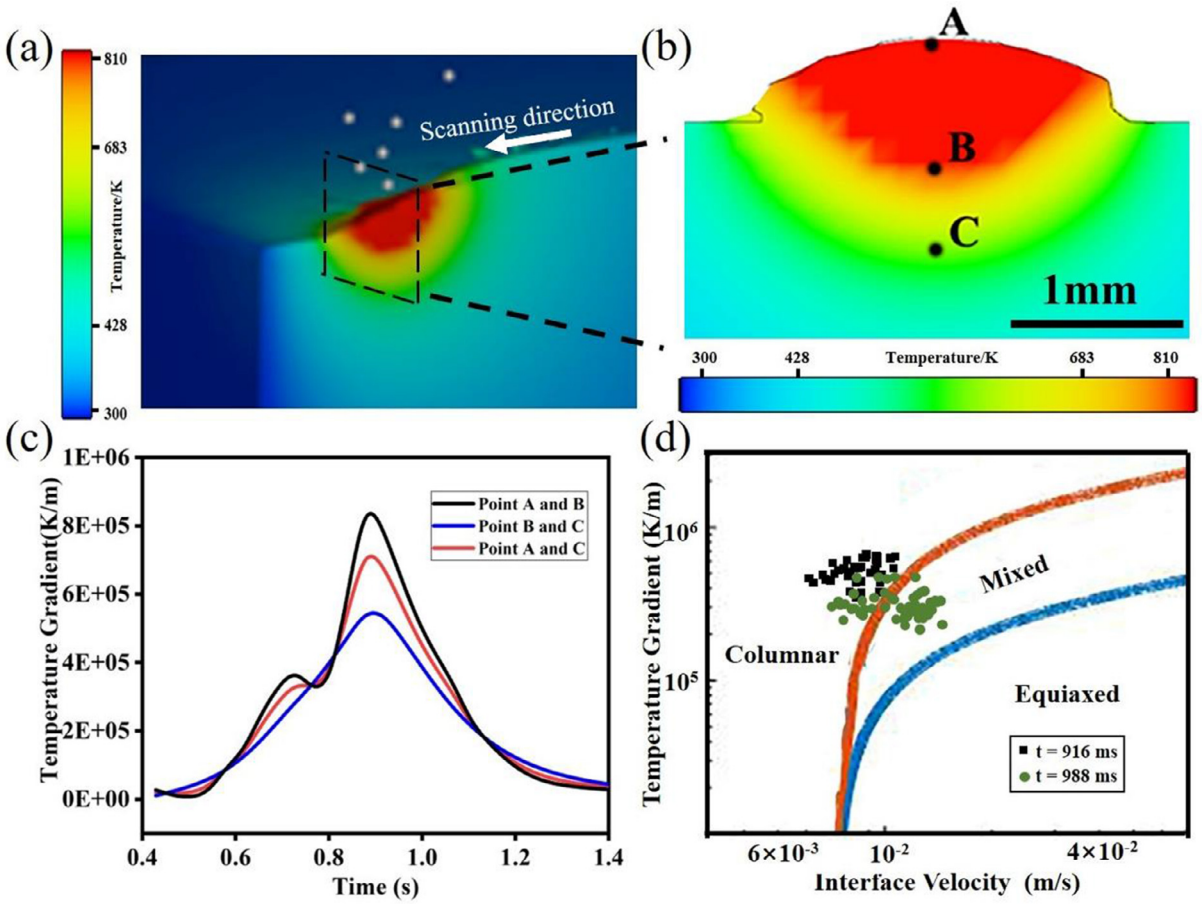

Fig. 5. Simulation results of single-track AlSi10Mg/TiB2 composite under 900 W blue laser at 4 mm/s: (a) 3D temperature distribution diagram, (b) temperature distribution in the cross-section view at t = 916 ms, (c) temperature gradient G between the reference points varying with the time, (d) G-R solidification map showing temporal evolution temperature gradient (G) *versus* solid/liquid interface velocity (R) for locations in the molten pool of blue laser deposition. Point A is the top of the molten pool, Point B is the bottom of the molten pool at 988 ms, and Point C is the bottom of the molten pool at 916 ms. The distance between point A and B is 735 μm, and the distance between points B and C is 552 μm.

Fig. 5(c) shows that the maximum temperature gradient between the top and bottom of the molten pool is 8×10^5 K/m. In particular, the temperature gradient in BL-DED is affected by the uniform energy distribution of the flat-top blue laser. To this end, we established a G-R diagram based on BL-DED of AlSi10Mg/TiB2 composite. Fig. 5(d) illustrates the G-R solidification map in the molten pool of blue laser deposition. The solid lines represent boundaries among columnar, mixed and equiaxed grains. At time t = 916 ms, that is the initial stage of solidification, the largest value of G is 8×10^5 K/m. At t = 988 ms, the largest value of G is 5.1×10^5 K/m. In addition, the solidification rate at the top of the molten pool increases between 916 ms to 988 ms. At t = 988 ms, G-R pairs have moved from the columnar to columnar-equiaxed mixed region due to smaller Gs and larger Rs.

In the DED process, the solidification process is initially oriented directionally from the S/L interface boundary, and columnar grains generally grow perpendicular to the S/L interface in laser melted single tracks at the initial stage [34]. However, the G gradually decreases and R increases as the solidification process continues, which is instrumental in the nucleation of equiaxed grains. In this study, the blue laser has a flat-top distribution, which means a relatively more uniform distribution of laser power density than that of the infrared laser. The difference of temperature between the top surface and the bottom of the molten pool is relatively smaller, producing lower temperature gradients. Lowering the temperature gradients with blue laser leads to a higher nucleation frequency and contributes to the formation of equiaxed grains, producing higher mechanical properties through grain-boundary strengthening. The grain size is significantly affected by the cooling rate in DED process. A higher cooling rate results in finer grain structure because only a short time is available for grain growth. Therefore, as the scanning speed increases, the average grain size of the molten pool decreases. Besides, reducing the thermal difference between the boundary and center of the melt pool could also stabilize the heat and mass transport, which is conducive to reducing the spatters in the manufacturing process and the porosity in the structure of materials [37,38].

4. Conclusion

Here we investigate the single tracks of AlSi10Mg/TiB2 composite made by high-power blue and infrared lasers at a laser power of 900 W at several different scanning speeds. Higher forming efficiency using a blue laser has been achieved due to higher absorption. EBSD results show a distinct transition from columnar to equiaxed grains in the cross-section view of the molten pool of BL-DED. In particular, the area fraction of equiaxed grains accounts for as high as 63% at 900 W blue laser and 4 mm/s, producing a very high area fraction of equiaxed grains in a DED single-track. Such a high fraction of equiaxed grains is mainly due to the low thermal gradients of the flat-top blue laser and the refining effect of nano TiB2 particles. The mathematical model validates that G-R pairs have moved from the columnar to the mixed columnar-equiaxed region during the solidification process of BL-DED due to the decreasing Gs and increasing Rs.

Supplementary materials

Supplementary material associated with this article can be found, in the online version.

Declaration of Competing Interest

The authors declare that they have no known competing financial interests or personal relationships that could have appeared to influence the work reported in this paper.

Data availability

No data was used for the research described in the article.

Acknowledgement

This work is sponsored by the National Natural Science Foundation of China (52075327, 52004160 and 52105469), Shanghai Sailing Program (20YF1419200), Natural Science Foundation of Shanghai (20ZR1427500), China Postdoctoral Science Foundation (2021M692038), Major Science and Technology Project of Huaibei (Z2020001) and the innovation foundation of Commercial Aircraft Manufacturing Engineering Center of China (No. 3-0410300-031). CLAL and PDL are grateful for the support under EPSRC (EP/P006566/1, EP/W003333/1, EP/V061798/1, EP/R511638/1, EP/W006774/1) and a RAEng Chair in Emerging Technologies (CiET1819–10). CLAL is grateful for the support under EP/W037483/1 and PDL is grateful for the support under EP/T02593X/1. This project has received funding from the European Union's Horizon 2020 research and innovation program under the Marie Sklodowska-Curie grant agreement No 896742.

Supplementary materials

Supplementary material associated with this article can be found, in the online version, at doi:10.1016/j.addlet.2023.100127.

References

[1] L. Yang, O. Harrysson, H. West, D. Cormier, Compressive properties of Ti–6Al–4V auxetic mesh structures made by electron beam melting, Acta Mater. 60 (8) (2012) 3370–3379.
[2] W. Yan, W. Ge, J. Smith, S. Lin, O.L. Kafka, F. Lin, W.K. Liu, Multi-scale modeling of electron beam melting of functionally graded materials, Acta Mater. 115 (2016) 403–412.
[3] B.K. Panda, S. Sahoo, Thermo-mechanical modeling and validation of stress field during laser powder bed fusion of AlSi10Mg built part, Results Phys. 12 (2019) 1372–1381.
[4] J.C. Haley, J.M. Schoenung, E.J. Lavernia, Observations of particle-melt pool impact events in directed energy deposition, Addit. Manuf. 22 (2018) 368–374.
[5] T. DebRoy, H.L. Wei, J.S. Zuback, T. Mukherjee, J.W. Elmer, J.O. Milewski, A.M. Beese, A. Wilson-Heid, A. De, W. Zhang, Additive manufacturing of metallic components – process, structure and properties, Prog. Mater Sci. 92 (2018) 112–224.
[6] J. Bi, Z. Lei, Y. Chen, X. Chen, X. Qin, Z. Tian, Effect of process parameters on formability and surface quality of selective laser melted Al-Zn-*Sc*-Zr alloy from single track to block specimen, Opt. Laser Technol. 118 (2019) 132–139.
[7] A. Wang, H. Wang, Y. Wu, H. Wang, 3D printing of aluminum alloys using laser powder deposition: a review, Int. J. Adv. Manuf. Technol. 116 (1–2) (2021) 1–37.
[8] K. Asano, M. Tsukamoto, Y. Sechi, Y. Sato, S.-i. Masuno, R. Higashino, T. Hara, M. Sengoku, M. Yoshida, Laser metal deposition of pure copper on stainless steel with blue and IR diode lasers, Opt. Laser Technol. 107 (2018) 291–296.
[9] Y. Sato, M. Tsukamoto, T. Shobu, Y. Funada, Y. Yamashita, T. Hara, M. Sengoku, Y. Sakon, T. Ohkubo, M. Yoshida, N. Abe, In situ X-ray observations of pure-copper layer formation with blue direct diode lasers, Appl. Surf. Sci. 480 (2019) 861–867.
[10] H. Wang, Y. Kawahito, R. Yoshida, Y. Nakashima, K. Shiokawa, Development of a high-power blue laser (445nm) for material processing, Opt. Lett. 42 (12) (2017) 2251–2254.
[11] F. Dausinger, J. Shen, Energy coupling efficiency in laser surface treatment, ISIJ Int. 33 (9) (1993) 925–933.
[12] V. Manvatkar, A. De, T. DebRoy, Heat transfer and material flow during laser assisted multi-layer additive manufacturing, J. Appl. Phys. 116 (12) (2014).
[13] J. Gu, S. Yang, M. Gao, J. Bai, Y. Zhai, J. Ding, Micropore evolution in additively manufactured aluminum alloys under heat treatment and inter-layer rolling, Mater. Des. 186 (2020).
[14] C.L.A. Leung, I. Elizarova, M. Isaacs, S. Marathe, E. Saiz, P.D. Lee, Enhanced near-infrared absorption for laser powder bed fusion using reduced graphene oxide, Appl. Mater. Today 23 (2021).
[15] T.V. Thejaswi, U. Tumkur, Rongpei Shi, Philip J. Depond, S.W. Tien, T. Roehling, Michael F. Crumb, John D. Roehling, Gabe Guss, M.J.M. Saad, A. Khairallah, Non-diffractive beam shaping for enhanced optothermal control in additive manufacturing, Sci. Adv. 7 (38) (2021).
[16] T.T. Roehling, R. Shi, S.A. Khairallah, J.D. Roehling, G.M. Guss, J.T. McKeown, M.J. Matthews, Controlling grain nucleation and morphology by laser beam shaping in metal additive manufacturing, Mater. Des. 195 (2020).
[17] R. Higashino, Y. Sato, S.-.I. Masuno, T. Shobu, Y. Funada, N. Abe, M. Tsukamoto, H. Helvajian, B. Gu, H. Chen, Development of blue diode laser for additive manufacturing, Laser 3D Manufacturing VII, 2020.
[18] B. Rethfeld, D.S. Ivanov, M.E. Garcia, S.I. Anisimov, Modelling ultrafast laser ablation, J. Phys. D Appl. Phys. 50 (19) (2017).
[19] H. Yang, J. Wu, Q. Wei, Z. Tang, A. Wang, X. Jin, X. Li, Y. Wu, G. Lu, H. Wang, H. Wang, Stable cladding of high reflectivity pure copper on the aluminum alloy substrate by an infrared-blue hybrid laser, Additive Manuf. Lett. 3 (2022).
[20] R. Indhu, V. Vivek, L. Sarathkumar, A. Bharatish, S. Soundarapandian, Overview of laser absorptivity measurement techniques for material processing, Lasers Manuf. Mate. Process. 5 (4) (2018) 458–481.
[21] A. Das, R. Fritz, M. Finuf, I. Masters, Blue laser welding of multi-layered AISI 316L stainless steel micro-foils, Opt. Laser Technol. 132 (2020).
[22] L.S.S.W. Britten, Blue high-power laser sources for processing solutions in e-mobility and beyond, Procedia CIRP 94 (2020) 592–595.
[23] P. Kiani, A.D. Dupuy, K. Ma, J.M. Schoenung, Directed energy deposition of AlSi10Mg: single track nonscalability and bulk properties, Mater. Des. 194 (2020).
[24] U. Scipioni Bertoli, A.J. Wolfer, M.J. Matthews, J.-P.R. Delplanque, J.M. Schoenung, On the limitations of volumetric energy density as a design parameter for selective laser melting, Mater. Des. 113 (2017) 331–340.
[25] Y. Zhang, Y. He, X. Li, L. Xiang, S. To, Error analysis of Gaussian spot width measured with CCD sensor, 6th International Symposium on Advanced Optical Manufacturing and Testing Technologies: Optical Test and Measurement Technology and Equipment, 2012.
[26] S. Luo, B. Lü, Propagation of the kurtosis parameter of elegant Hermite-Gaussian and Laguerre-Gaussian beams passing through ABCD systems, Optik (Stuttg) 113 (5) (2002) 227–231.
[27] H. Wang, Y. Kawahito, R. Yoshida, Y. Nakashima, K. Shiokawa, A model to calculate the laser absorption property of actual surface, Int. J. Heat Mass Transf. 118 (2018) 562–569.
[28] W. Yan, W. Ge, Y. Qian, S. Lin, B. Zhou, W.K. Liu, F. Lin, G.J. Wagner, Multi-physics modeling of single/multiple-track defect mechanisms in electron beam selective melting, Acta Mater. 134 (2017) 324–333.
[29] Y. Liu, J. Zhang, Q. Tan, Y. Yin, S. Liu, M. Li, M. Li, Q. Liu, Y. Zhou, T. Wu, F. Wang, M.-.X. Zhang, Additive manufacturing of high strength copper alloy with heterogeneous grain structure through laser powder bed fusion, Acta Mater. 220 (2021).
[30] R. Shi, S.A. Khairallah, T.T. Roehling, T.W. Heo, J.T. McKeown, M.J. Matthews, Microstructural control in metal laser powder bed fusion additive manufacturing using laser beam shaping strategy, Acta Mater. 184 (2020) 284–305.
[31] T.T. Roehling, S.S.Q. Wu, S.A. Khairallah, J.D. Roehling, S.S. Soezeri, M.F. Crumb, M.J. Matthews, Modulating laser intensity profile ellipticity for microstructural control during metal additive manufacturing, Acta Mater. 128 (2017) 197–206.
[32] R.R. Dehoff, M.M. Kirka, W.J. Sames, H. Bilheux, A.S. Tremsin, L.E. Lowe, S.S. Babu, Site specific control of crystallographic grain orientation through electron beam additive manufacturing, Mater. Sci. Technol. 31 (8) (2014) 931–938.
[33] J.A. Spittle, Columnar to equiaxed grain transition in as solidified alloys, Int. Mater. Rev. 51 (4) (2013) 247–269.
[34] V. Ocelík, I. Furár, J.T.M. De Hosson, Microstructure and properties of laser clad coatings studied by orientation imaging microscopy, Acta Mater. 58 (20) (2010) 6763–6772.
[35] Y.K. Xiao, H. Chen, Z.Y. Bian, T.T. Sun, H. Ding, Q. Yang, Y. Wu, Q. Lian, Z. Chen, H.W. Wang, Enhancing strength and ductility of AlSi10Mg fabricated by selective laser melting by TiB2 nanoparticles, J. Mater. Sci. Technol. 109 (2022) 254–266.
[36] J.D. Hunt, Steady state columnar and equiaxed growth of dendrites and eutectic, Mater. Sci. Eng 1 (1984) 75–83.
[37] S.A. Khairallah, A.T. Anderson, A. Rubenchik, W.E. King, Laser powder-bed fusion additive manufacturing: physics of complex melt flow and formation mechanisms of pores, spatter, and denudation zones, Acta Mater. 108 (2016) 36–45.
[38] P. Wei, Z. Wei, Z. Chen, Y. He, J. Du, Thermal behavior in single track during selective laser melting of AlSi10Mg powder, Appl. Phys. A 123 (9) (2017).